Two-dimensional tellurene nanosheets as saturable absorber of passively *Q*-switched Nd:YAG solid-state laser

Tianhong Tang (唐天鸿)[1], Fang Zhang (张 芳)[1], Mengxia Wang (王梦霞)[1], Zhengping Wang (王正平)[1,2,*], and Xinguang Xu (许心光)[1,2,]**

[1]*State Key Laboratory of Crystal Materials, Shandong University, Jinan 250100, China*
[2]*Key Laboratory of Functional Crystal Materials and Device (Shandong University), Ministry of Education, Jinan 250100, China*
**Corresponding author: zpwang@sdu.edu.cn; **corresponding author: xgxu@sdu.edu.cn*
Received November 23, 2019; accepted December 26, 2019; posted online April 14, 2020

For the first time, a group-VI single element nanomaterial was used as the optical saturable absorber (SA) to generate laser pulses. With two-dimensional (2D) tellurene as a passive *Q*-switch, 1.06 μm and 1.3 μm pulse laser operations were realized from a diode-pumped Nd:YAG crystal. The shortest pulse widths were 98 ns and 178 ns, and the highest peak powers were 2.68 W and 2.45 W, respectively. Our research determines that tellurene is an excellent SA material in the near-infrared region.

Keywords: tellurene; nanosheets; absorber; graphene; passive Q-switching.
doi: 10.3788/COL202018.041403.

Since graphene appeared to the public in 2004, two-dimensional (2D) nanomaterials have refreshed people's traditional viewpoints and opened a new world[1]. Afterward, many 2D nanomaterials like topological insulators (TIs)[2,3], transition-metal dichalcogenides (TMDs)[4], and mono-elementals[5–7] have been proposed and developed forming a global research hotspot. Their remarkable physical, chemical, and biological properties attract wide attention. Among these materials, the group III, IV, and V elements represented by black phosphorus (BP) have made great progress, with advantages of a tunable electronic bandgap by thickness[8,9], a high carrier mobility[10], and strong intrinsic in-plane anisotropy . However, for BP, there are some inevitable problems, like poor environment stability, that have seriously limited its applications. Different from the group III, IV, and V elements whose 2D materials have been predicted and fabricated very early[7,9,11,12], the nanostructure of group VI element tellurium (Te) was mostly synthesized in one-dimensional (1D) nanotube form[13–15], due to its inherent structural anisotropy. The earliest 2D Te was reported in 2017[16]. It exhibited some outstanding merits like environment stability and low synthetic cost as well as excellent nonlinear optical characteristics[17].

As a single element in group VI, Te has a distinct chair-chain crystal lattice. The van der Waals-type bond makes the chains of Te atoms stack together, surrounding the axes in the center and corners of the hexagonal elementary cell that are parallel to the [0001] direction[18]. The Te atoms in each chain have covalent bonds with the closest two neighbors. Some earlier researchers have found that bulk Te has a high hole mobility ($\sim 105\ \mathrm{cm^2 \cdot V^{-1} \cdot s^{-1}}$)[19] and a small effective mass due to spin-orbit coupling[20], which means the saturable absorption is very likely to occur. The absorption abilities of tellurene cover ionization, atoms, and gas molecules[21,22]. At the same time, Te has a tunable bandgap that changes from 0.31 eV (bulk) to 1.17 eV (2 layers) by adjusting the thickness[19]. In addition, Te possesses prominent photoconductivity[23], thermoelectricity[24], and piezoelectricity[25], which is helpful for carrier transfer, desorption of adsorbate, etc.[22]. These superior properties mean that Te can be applied in many fields such as photoelectric detectors and sensors.

Previously, a Z-scan method was used to explore the nonlinear optical property of Te dispersion liquid, which proves that 2D Te has a notable saturable absorber (SA) behavior in the near-infrared band of 1064–1700 nm (i.e., 1.17–0.73 eV)[17]. In this Letter, large area, high-quality 2D Te nanosheets of a few layers thickness were fabricated from bulk Te by the liquid-phase-exfoliation (LPE) method. The nonlinear transmittance of Te thin film was characterized with a 1064 nm laser. By fitting the experimental data, the saturation intensity and modulation depth were determined to be 0.87 $\mathrm{MW/cm^2}$ and 6.3%, respectively. With Te thin film as the saturable absorber and Nd:YAG crystal as the gain medium, low threshold, narrow pulse width passively *Q*-switched laser operations were achieved at 1.06 μm and 1.3 μm. A maximum average output power of 140 mW was obtained from the 1.06 μm laser experiment, corresponding to a repetition frequency of 535.8 kHz, pulse width of 97.5 ns, and peak power of 2.68 W.

The few-layer tellurene nanosheets were manufactured from bulk Te by using the LPE method. The experimental samples of different stages are shown in Fig. 1. First, we put 160 mg bulk tellurium with a small amount of absolute ethanol into an agate mortar, and grinded for 4 h.

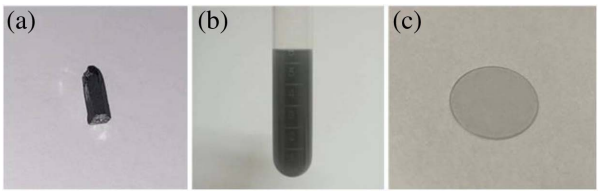

Fig. 1. (a) Original bulk tellurium crystal, (b) prepared tellurene nanosheets dispersion liquid, and (c) tellurene nanosheets SA-coated sapphire substrate.

The absolute ethanol was used for preventing oxidation with air and better grinding, which could ensure the sample purity. Then, the grinded powder was dissolved in absolute ethanol and stirred for 2 min. Next, the sample was put in an ultrasonic device to pulverize for 3 h. The obtained dispersion liquid was settled for 72 h to precipitate large tellurene grains as much as possible. After removing the deposition, the rest of the supernatant liquor was stored in a centrifuge tube and used for various characterization tests. At the same time, a part of the supernatant liquor was coated on a sapphire substrate to serve as the saturable absorber of the solid-state laser.

To observe the morphology of bulk tellurium crystal and 2D tellurene nanosheets, a scanning electron microscope (SEM) measurement was carried out. As shown in Fig. 2(a), the edge of the tellurium crystal displays an obvious stratified structure. Figure 2(b) displays the typical surface profile of prepared tellurene nanosheets. Because the binding force between the layers was weak, the few-layer tellurene was successfully exfoliated, and the almost-transparent appearance was due to the ultra-thin nature.

Atomic force microscopy (AFM, Nanoscope Multi Mode V, Digital Instruments/Bruker systems) was used to measure the 3D topography of the tellurene thin film, as shown in Figs. 3(a) and 3(b). The prepared tellurene dispersion was deposited onto a polished sapphire substrate and then dried for 12 h before AFM measurement. A typical cross section of the tellurene thin film was selected to analyze the sample thickness. As seen in Fig. 3(b), the average thickness of the nanosheets was about 4 nm. Considering the thickness of the single-layer tellurene was 0.41 nm[26], the layer number of the as-prepared 2D Te nanosheets was estimated to be 10 or so. Figure 3(c) is the high-resolution transmission electron microscopy (HRTEM) image. No point defects or

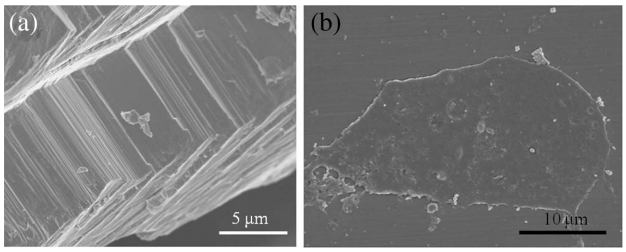

Fig. 2. SEM images of (a) the bulk tellurium crystal and (b) the exfoliated tellurene nanosheet.

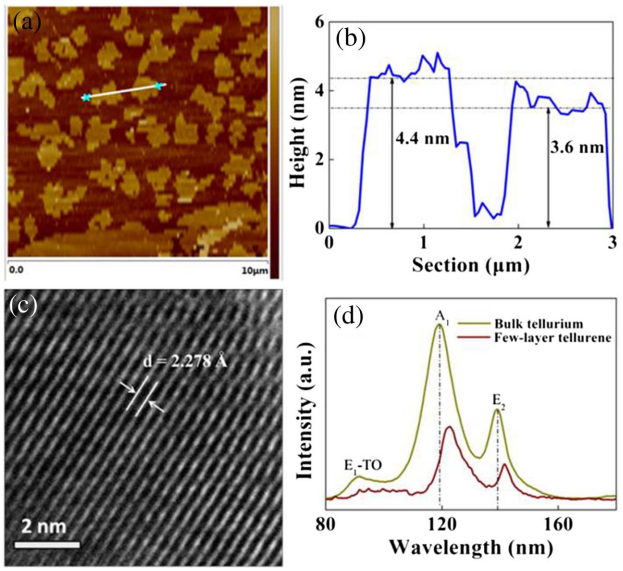

Fig. 3. Characterizations of the tellurene thin film. (a) AFM image, (b) height profile, (c) HRTEM image, and (d) Raman spectrum.

dislocations were observed over a large area within the tellurene flake, and clear lattice fringes were presented, which indicated that the as-prepared tellurene had a high quality. The distance d between adjacent lattice fringes was 2.278 Å (1 Å = 0.1 nm), corresponding to the (110) plane[27].

To further explore the structure information of the tellurene thin film, we carried out a Raman spectrum measurement. The excitation wavelength, confocal aperture, and objective were 532 nm, 200 μm, and 100×, respectively. As shown in Fig. 3(d), the Raman spectrum of bulk tellurium has three principal Raman-active modes, i.e., A_1, $E_1 - TO$, and E_2, which locate at the wavenumbers of 119.3 cm^{-1}, 91.6 cm^{-1}, and 139.1 cm^{-1}, respectively. The absence of the $E_1 - LO$ mode is coincident with the previous reports[28–30]. The E_1 mode will gradually disappear when the layer number of the sample decreases to a few layers (approximately thinner than 15 nm)[26]. For our tellurene thin film, the same tendency is presented in Fig. 3(d), at the same time the A_1 and E_2 modes exhibit blueshifts, which locate at 122.9 cm^{-1} and 141.6 cm^{-1}, respectively. This property is quite different with other 2D van der Waals materials, which show a redshift when their layer numbers decrease[31–33]. It may be attributed to the distinct chiral-chain van der Waals structure of tellurene. In short, in the Raman spectrum, the disappearance of the E_1 mode and the blueshifts of A_1 and E_2 modes have further confirmed that the experimental sample is a few-layer tellurene.

The linear transmission spectrum of the as-prepared tellurene saturable absorber was recorded by a UV/VIS/NIR spectrophotometer (U-3500, Hitachi, Japan), as shown in Fig. 4(a). A blank sapphire substrate was used as the reference for calculating the net transmittance of the tellurene thin film. The measured wavelength range was

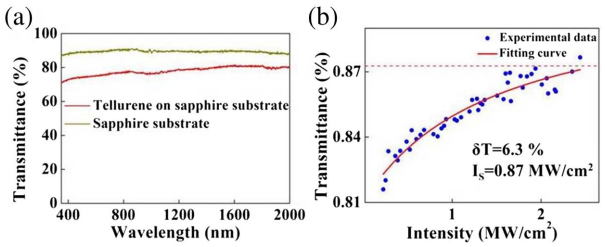

Fig. 4. (a) Linear transmission spectrum of the tellurene SA and (b) the nonlinear transmittance of the tellurene thin film.

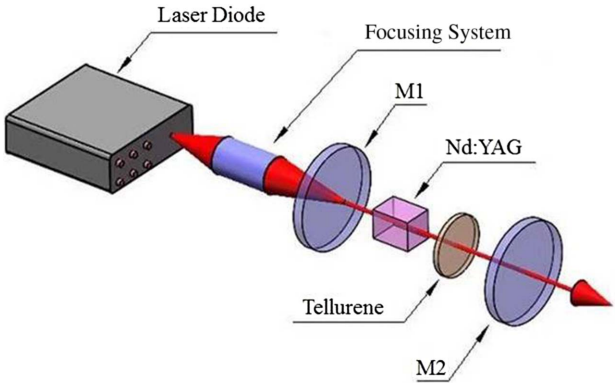

Fig. 5. Schematic diagram of the passively Q-switched laser based on the tellurene.

350–2000 nm. At 1064 nm, the transmittances of the tellurene SA on the sapphire substrate and the blank sapphire substrate were 77.3% and 89.5%, respectively. Thus, the net transmittance of the tellurene thin film was about 86.4%, corresponding to a relatively large sample loss of 13.6%.

The transmittance variation of the tellurene thin film at different incident powers is shown in Fig. 4(b), which can directly characterize its SA properties. An optical parametric oscillator (OPO) laser was used as the light source, which had an excitation wavelength, repetition frequency, and pulse duration of 1064 nm, 10 Hz, and 6 ns, respectively. The initial laser beam was reshaped with a diaphragm, and then converted to a facula with a diameter of 2.5 mm by a 2:1 optical compression system. The experimental data can be fitted by the formula[34]

$$T = A\exp\left(\frac{-\delta T}{1+\frac{I}{I_S}}\right),$$

where T is the transmittance of the sample, A is a normalization constant, δT is the absolute modulation depth, I is the incident intensity, and I_S is the saturation intensity. In Fig. 4(b), the influence of the sapphire substrate has been removed, i.e., the presented data were obtained by dividing the original data by the transmittance of the sapphire substrate (85% at 1064 nm). The saturation intensity of the tellurene thin film was fitted to be 0.87 MW/cm^2, and the absolute modulation depth was 6.3% (from 81.3% to 87.6%)

In a previous report[17], the modulation depth for ~4 nm few-layer tellurene at 1.06 μm is 30% and the saturation intensity is 29.93 MW/cm^2, which are much different from the present results. The main reason is that the sample conditions are different. In Ref. [17], the SA medium is a 2D Te dispersion liquid, which possesses a much longer interaction distance (2 mm) than the present 2D Te thin film. The large interaction distance and high Te nanosheets concentration have led to a larger modulation depth and a higher saturation intensity. The damage threshold of the tellurene nanosheets at 1064 nm is measured to be 105.3 MW/cm^2. The high initial transmittance and small saturation intensity are favorable for low-threshold Q-switched operations. At an intensity of 2.4 MW/cm^2, the remaining loss of the tellurene SA is 12.4%.

The experimental setups of the 1.06 μm and 1.3 μm lasers were similar, as shown in Fig. 5. The pump source was a commercial fiber-coupled laser-diode. Its central wavelength was 808 nm, and the core diameter and numerical aperture of the coupled fiber were 100 μm and 0.22, respectively. The pump beam was delivered into the laser crystal by a 1:1 optical collimation system. A 0.4 at.% doped Nd:YAG crystal was used as the gain medium which had its strongest emission peaks at 1.06 μm and 1.3 μm. The crystal dimensions were 4 mm × 4 mm× 7 mm, and the crystal end-faces were anti-reflection (AR)-coated at 0.9–1.1 μm. The Nd:YAG crystal was wrapped in an indium foil and held in a copper block to relieve the thermal load, and the copper block was cooled by circulating water with a fixed temperature of 15°C. The passive Q-switch was a tellurene SA, as exhibited in Fig. 1(c). The laser resonator was composed of a flat mirror M1 and a concave mirror M2. The flat mirror M1 was AR-coated at 808 nm and high-reflection-coated at the working wavelength. The concave mirror M2 was employed as an output coupler with a partial transmittance at the working wavelength. Under our experimental conditions, the optimized passively Q-switched (PQS) parameters of M2 were $T = 10\%$, $R = 100$ mm at 1.06 μm, and $T = 5\%$, $R = 200$ mm at 1.34 μm, respectively. Here, T was the transmittance at the working wavelength and R was the curvature radius. The cavity lengths for all of the laser experiments were kept at 25 mm. A power meter (Powermax 500D, Molectron Inc.) was used to measure the average output power, and the temporal behaviors of the laser pulses were recorded by a digital oscilloscope (DPO7104, Tektronix Inc.) with a photodiode detector (Model 1621, New Focus, response time 1 ns, decay time 1.5 ns).

The continuous-wave (CW) laser output could be achieved by removing the SA from the resonator; the passively Q-switched operation was realized by inserting the tellurene SA into the resonator. The experimental results are demonstrated in Figs. 6 and 7, corresponding to the laser operations at 1.06 μm and 1.34 μm, respectively.

The variation of 1.06 μm average output power with absorbed pump power is depicted in Fig. 6(a). When the absorbed pump power was 1.67 W, the maximum CW and PQS output powers were 0.89 W and

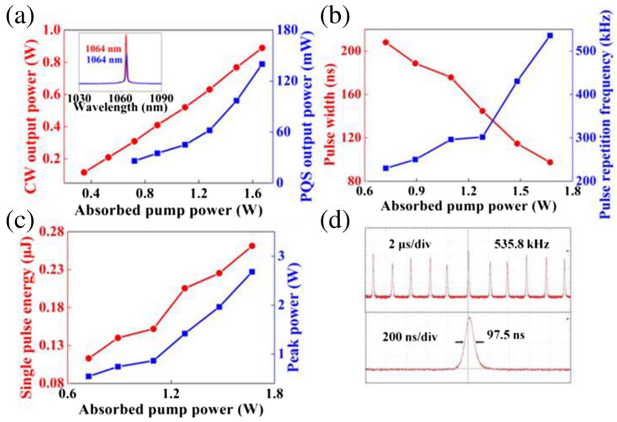

Fig. 6. 1064 nm passively Q-switched laser characteristics of the tellurene SA. (a) The CW and PQS output powers. The inset shows the CW and PQS laser emission spectra. (b) The pulse duration and repetition frequency. (c) The single-pulse energy and peak power. (d) The pulse train and single-pulse profile.

140 mW, respectively, and the corresponding threshold absorbed pump powers were 0.21 and 0.72 W, which coincided with the high initial transmittance of the tellurene SA. The PQS laser operation could be obtained in the pump region of 0.72–1.67 W. When the pump power further increased, the pulse performance degraded rapidly. The inset of Fig. 7(a) is the emission spectra of the CW and PQS lasers, which were measured by an optical spectrum analyzer (HR4000, Ocean Optics). The central wavelength is located at 1064 nm. The 1.06 μm pulse characteristics are shown in Figs. 6(b)–6(d). The pulse repetition frequency, single pulse energy, and peak power increased with the elevating of the pump power, while the pulse duration varied in an opposite tendency. When the pump power was 1.67 W, the shortest pulse duration of 97.5 ns was obtained, and the corresponding pulse repetition frequency, single pulse energy, and peak power were 535.8 kHz, 0.26 μJ, and 2.68 W, respectively. Figure 6(d) presents the pulse train and single pulse profile at this moment. The amplitude fluctuation instability of the pulses train was ±5%. During the whole 1.06 μm PQS laser experiment, no obvious damage was observed from the tellurene SA.

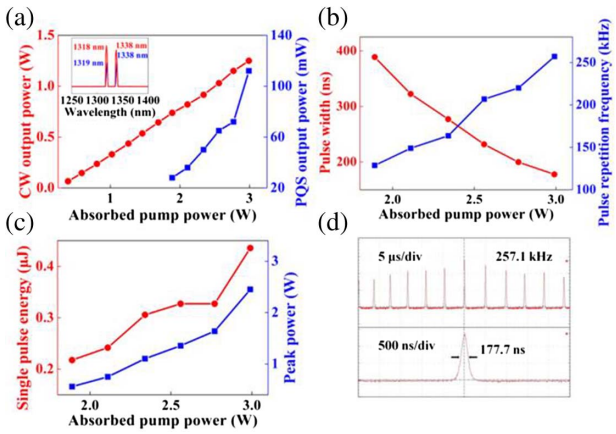

Fig. 7. 1.3 μm dual-wavelength passively Q-switched laser characteristics of the tellurene SA. (a) The CW and PQS output powers. The inset is the CW and PQS laser emission spectra. (b) The pulse duration and repetition frequency. (c) The single-pulse energy and peak power. (d) The pulse train and single-pulse profile.

The 1.3 μm laser experimental results are summarized in Fig. 7. Comparing with the 1.06 μm laser operation, the threshold pump power of the 1.3 μm PQS laser operation increased to 1.89 W. The main reason was that the emission cross section of the 1.3 μm (8.7×10^{-20} cm^2 at 1319 nm, 9.2×10^{-20} cm^2 at 1338 nm) was much smaller than that of the 1.06 μm (45.8×10^{20} cm^2 at 1,064 nm) in Nd:YAG crystal[35]. As shown in Fig. 7(a), the maximum CW and PQS output powers were achieved at an absorbed pump power of 2.99 W, which were 1.25 W and 112 mW, respectively. The 1.3 μm CW and PQS output spectra are presented in the inset of Fig. 7(a) (Series No. s00655-05A1, Wavecheck IR). There were two wavelengths, 1319 and 1338 nm, corresponding to different energy level transitions in Nd:YAG crystal, i.e., $R_2(^4F_{3/2}) \rightarrow X_1(^4I_{13/2})$ and R_2 $(^4F_{3/2}) \rightarrow X_3$ $(^4I_{13/2})$, respectively[35].

The characteristics of the 1.3 μm pulse laser are displayed in Figs. 7(b)–7(d). The shortest pulse width of 177.7 ns was obtained at an absorbed pump power of 2.99 W; and the largest single-pulse energy and the highest peak power were 0.44 μJ and 2.45 W, respectively. At the highest pulse repetition frequency of 257.1 kHz, the amplitude fluctuation instability of the pulses train was ±11%, as shown in Fig. 7(d).

In the passively Q-switched laser experiments, the variation range of the maximum average output power in half an hour was 132–140 mW for the 1.06 μm laser operation, and 107–112 mW for the 1.3 μm laser operation. The corresponding long-term instabilities of average output powers were ±2.9% and ±2.3%, respectively. In addition, the output beam distribution of the 1.06 μm pulse laser was measured by a CCD camera (Coherent, LaserCam-HR II), and the result is shown in Fig. 8. It shows that the output laser possesses a symmetrical Gaussian distribution with the TEM_{00} fundamental transverse mode. Comparing with other 2D material Q-switched lasers[36–38], the beam quality of the present laser is comparable.

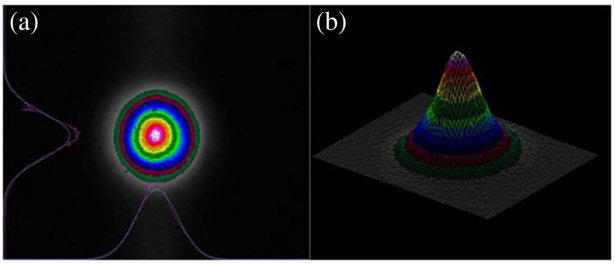

Fig. 8. (a) 2D and (b) 3D facula profile of the passively Q-switched 1.06 μm laser.

In Table 1, we compare the PQS solid-state laser performances of tellurene nanosheets and other representative 2D nanomaterials. It shows that either for the 1.06 μm or for the 1.3 μm laser operation, the tellurene displays the advantages of a low pump threshold, short pulse width, high peak power, and high repetition frequency. The listed data indicate that tellurene is an excellent 2D saturable absorption material for the pulse modulation of near-infrared lasers. Generally, for 2.0 μm PQS laser operation, 2D nanomaterials present a higher pump threshold, lower repetition frequency, and wider pulse width than those for a 1 μm laser, as shown in Table 1. It has been found that the SA properties of tellurene nanosheets increase with the increase of wavelength[17]. Associating with the wide transmittance band, low saturation intensity, moderate modulation depth, and high stability, one can expect that tellurene nanosheets may be a promising 2D SA material for 2 μm solid-state lasers.

In present experiments, with respect to the CW output power, the *Q*-switched optical conversion efficiency is 15.7% for 1.06 μm laser operations, and 9% for 1.3 μm laser operations. It indicates that the SA component still has a large non-saturable loss, just as Fig. 4 has shown. In addition, the pump absorption efficiency of the Nd:YAG laser crystal is only 50% or so, and the residual unabsorbed pump power will cause a severe thermal effect on the SA component, which is also one of the reasons for the low optical conversion efficiencies. In short, by further optimizing the preparation technique of the SA and the experimental conditions, the overall performance of the *Q*-switched laser is expected to be greatly improved, including a larger average output power, shorter pulse duration, higher pulse peak power, etc.

Limited by the experimental conditions and detecting equipment, we can not perform a mode-locking laser experiment at the present stage. Nevertheless, tellurene nanosheets are an excellent 2D SA material, and are very promising for use in mode-locking operations to achieve ultrafast laser pulses.

For the first time, a 2D nanomaterial prepared from a group VI element, tellurium, was used as the SA of a passively *Q*-switched laser. The few-layer tellurene nanosheets were exfoliated from bulk tellurium crystals using the liquid phase exfoliation method. By AFM measurement, their thickness was determined to be 4 nm or so, approximately corresponding to 10 layers of nanosheets. The Raman spectrum further confirmed their few-layer structure. With tellurene thin film as the SA, the passively *Q*-switched operations were realized for the 1.06 μm and 1.3 μm solid-state lasers. The best experimental results came from the 1.06 μm laser *Q*-switching, including the shortest pulse width of 97.5 ns, the largest repetition frequency of 535.8 kHz, and the highest peak power of 2.68 W. Thus, the reliable environment stability, low synthesis cost, and excellent nonlinear optical properties enable Te to be a promising SA material. This research shows that tellurene is a stable, low cost, and promising

Table 1. Passively *Q*-switched Performance of Solid-state Laser for Different 2D Nanomaterials

		Pulse properties					
Wavelength (μm)	SA material	Pump threshold (W)	Average power (mW)	Repetition frequency (kHz)	Pulse width (ns)	Peak power (W)	Reference
1.06	Graphene	8.28	105	660	180.5	0.88	[39]
	BP	1.2	135	220	321	2	[40]
	MoS_2	1.23	227	732	970	0.32	[41]
	WS_2	1.49	201	481	112	3.72	[42]
	ReS_2	4.4	670	274	1080	2.3	[38]
	Tellurene	0.72	140	535.8	97.5	2.68	This work
1.3	Graphene	2.2	890	135	466	14.14	[43]
	BP	0.9	157	175	363	3	[40]
	MoS_2	6.9	52	77	729	0.93	[41]
	ReS_2	0.12	78	214	403	0.9	[44]
	Tellurene	1.89	112	257.1	177.7	2.45	This work
2.0	Graphene	5.6	37	27.9	2080	0.84	[45]
	BP	–	12	17.7	3100	0.0002	[46]
	MoS_2	1.65	100	48.09	800	2.59	[47]
	WS_2	2.75	381	44.2	5600	1.54	[48]
	ReS_2	1.15	245	677	415	0.87	[49]

2D SA material for the pulse modulation of near-infrared lasers.

This work was supported by the National Natural Science Foundation of China (No. 61975096), Basic Research and Free Exploration Project of Shenzhen City (No. JCYJ20180305164316517), and the Natural Science Foundation of Shandong Province (No. ZR2017MF031).

References

1. K. S. Novoselov, A. K. Geim, S. V. Morozov, D. Jiang, Y. Zhang, S. V. Dubonos, I. V. Grigorieva, and A. A. Firsov, Science **306**, 666 (2004).
2. J. E. Moore, Nature **464**, 194 (2010).
3. B. Guo, Chin. Opt. Lett. **16**, 20004 (2018).
4. Q. H. Wang, K. K. Zadeh, A. Kis, J. N. Coleman, and M. S. Strano, Nat. Nanotechnol. **7**, 699 (2012).
5. A. C. Gomez, L. Vicarelli, E. Prada, J. O. Island, K. L. Narasimha-Acharya, S. I. Blanter, D. J. Groenendijk, M. Buscaema, G. A. Steels, and J. V. Alvaree, 2D Materials **1**, 025001 (2014).
6. A. J. Mannix, X. F. Zhou, B. Kiraly, J. D. Wood, D. Alducin, B. D. Myers, X. L. Liu, B. L. Fisher, U. Santiago, J. R. Guest, M. J. Yacaman, A. Ponce, A. R. Oganov, M. C. Hersam, and N. P. Guisinger, Science **350**, 1513 (2015).
7. X. Wang, Z. F. Wang, Y. G. Wang, L. Li, G. W. Yang, and J. P. Li, Chin. Opt. Lett. **15**, 85 (2017).
8. L. K. Li, Y. J. Yu, G. J. Ye, Q. Q. Ge, X. D. Ou, H. Wu, D. L. Feng, and X. H. Chen, Nat. Nanotechnol. **9**, 372 (2014).
9. Y. Zheng, C. Y. Lan, Z. F. Zhou, X. Y. Hu, T. Y. He, and C. Li, Chin. Opt. Lett. **16**, 020006 (2018).
10. J. S. Qiao, X. H. Kong, Z. X. Hu, F. Yang, and W. Ji, Nat. Commun. **5**, 4475 (2014).
11. V. Tran, R. Soklaski, Y. F. Liang, and L. Yang, Phys. Rev. B. **89**, 235319 (2014).
12. P. Vogt, P. P. De, C. Quaresima, J. Avila, E. Frantzeskakis, M. C. Asensio, A. Resta, B. Ealet, and L. G. Le, Phys. Rev. Lett. **108**, 155501 (2012).
13. B. Mayers and Y. Xia, J. Mater. Chem. **12**, 1875 (2002).
14. M. S. Mo, J. H. Zeng, X. M. Liu, W. C. Yu, S. Y. Zhang, and Y. T. Qian, Adv. Mater. **14**, 1658 (2002).
15. H. S. Qian, S. H. Yu, J. Y. Gong, L. B. Luo, and L. F. Fei, Langmuir **22**, 3830 (2006).
16. Z. L. Zhu, X. L. Cai, S. Yi, J. L. Chen, Y. W. Dai, C. Y. Niu, Z. X. Guo, M. H. Xie, F. Liu, J. Cho, Y. Jia, and Z. Y. Zhang, Phys. Rev. Lett. **119**, 106101 (2017).
17. F. Zhang, G. Liu, Z. Wang, T. Tang, X. Wang, C. Wang, S. Fu, F. Xing, K. Han, and X. Xu, Nanoscale **11**, 17058 (2019).
18. A. V. Hippel, J. Chem. Phys. **16**, 372 (1948).
19. J. S. Qiao, Y. H. Pan, F. Yang, C. Wang, Y. Chai, and W. Ji, Sci. Bull. **63**, 159 (2018).
20. T. Doi, K. Nakao, and H. Kamimura, J. Phys. Soc. Jpn. **28**, 36 (1969).
21. X. H. Wang, D. W. Wang, A. J. Yang, N. Koratkar, J. F. Chu, P. L. Lv, and M. Z. Rong, Phys. Chem. Chem. Phys. **20**, 4058 (2018).
22. Y. S. Chen, J. Ding, X. M. He, J. Xu, and Y. Q. Feng, Microchim. Acta **185**, 368 (2018).
23. J. W. Liu, J. H. Zhu, C. L. Zhang, H.W. Liang, and S. H. Yu, J. Am. Chem. Soc. **132**, 8945 (2010).
24. T. I. Lee, S. Lee, E. Lee, S. Sohn, Y. Lee, S. Lee, G. Moon, D. Kim, Y. S. Kim, J. M. Myoung, and Z. L. Wang, Adv. Mater. **25**, 2920 (2013).
25. H. Peng and N. Kioussis, Phys. Rev. B. **89**, 195206 (2014).
26. Y. X. Wang, G. Qiu, R. X. Wang, S. Y. Huang, Q. X. Wang, Y. Y. Liu, Y. C. Du, W. A. Goddard III, M. J. Kim, X. F. Xu, P. D. Ye, and W. Z. Wu, Nat. Electron. **1**, 228 (2018).
27. P. Cherin and P. Unger, Acta Crystallogr. **23**, 670 (1967).
28. Q. S. Wang, M. Safdar, K. Xu, M. Mirza, Z. X. Wang, and J. He, ACS Nano **8**, 7497 (2014).
29. A. S. Pine and G. Dresselhaus, Phys. Rev. B. **17**, 3965 (1971).
30. Y. C. Du, G. Qiu, Y. X. Wang, M. W. Si, X. F. Xu, W. Z. Wu, and P. D. Ye, Nano Lett. **17**, 3965 (2017).
31. X. M. Wang, A. M. Jones, K. L. Seyler, V. Tran, Y. C. Jia, H. Zhao, H. Wang, L. Yang, X. D. Xu, and F. N. Xia, Nat. Nanotechnol. **10**, 517 (2015).
32. H. Liu, A. T. Neal, Z. Zhu, Z Luo, X. F. Xu, D. T. Nek, and P. D. Ye, ACS Nano **8**, 4033 (2014).
33. C. G. Lee, H. G. Yan, L. E. Brus, T. F. Heinz, J. Hone, and S. M. Ryu, ACS Nano **4**, 2695 (2010).
34. H. H. Yu, H. Zhang, Y. C. Wang, C. J. Zhao, B. L. Wang, S. C. Wen, H. J. Zhang, and J. Y. Wang, Laser Photon. Rev. **7**, L77 (2013).
35. S. Singh, R. G. Smith, and L. G. Van Uitert, Phys. Rev. B. **10**, 2566 (1974).
36. S. Han, X. L. Li, H. H. Xu, Y. G. Zhao, H. H. Yu, H. J. Zhang, Y. Z. Wu, Z. P. Wang, X. P. Hao, and X. G. Xu, Chin. Opt. Lett. **12**, 011401 (2014).
37. X. L. Sun, H. K. Nie, J. L. He, R. W. Zhao, X. C. Su, Y. R. Wang, B. T. Zhang, R. H. Wang, and K. J. Yang, IEEE J. Sel. Top. Quantum Electron. **24**, 1600405 (2018).
38. Y. C. Xue, L. Li, B. Zhang, R. X. Wang, H. Tian, J. H. Cui, F. J. Tian, and J. Z. Zhang, Opt. Commun. **445**, 165 (2019).
39. H. H. Yu, X. F. Chen, H. J. Zhang, X. G. Xu, X. B. Hu, Z. P. Wang, J. Y. Wang, S. D. Zhuang, and M. H. Jiang, ACS Nano **4**, 7582 (2010).
40. S. Han, F. Zhang, M. Wang, L. Wang, Y. Zhou, Z. Wang, and X. Xu, Indian J. Phys. **91**, 439 (2017).
41. S. X. Wang, H. H. Yu, H. J. Zhang, A. Z. Wang, M. W. Zhao, Y. X. Chen, L. M. Mei, and J. Y. Wang, Adv. Mater. **26**, 3538 (2014).
42. N. Zhang, T. Zhang, Y. H. Wang, and J. J. Song, Optik **127**, 7689 (2016).
43. H. B. Shen, Q. P. Wang, X. Y. Zhang, Z. J. Liu, F. Bai, Z. H. Cong, X. H. Chen, L. Gao, H. J. Zhang, X. G. Xu, S. R. Wei, and X. F. Chen, Appl. Phys. Express **5**, 092703 (2012).
44. M. X. Lin, Q. Q. Peng, W. Hou, X. W. Fan, and J. Liu, Opt. Laser Tech. **109**, 90 (2019).
45. Q. Wang, H. Teng, Y. W. Zou, Z. G. Zhang, D. H. Li, R. Wang, C. Q. Gao, J. J. Lin, L. W. Guo, and Z. Y. Wei, Opt. Lett. **37**, 395 (2012).
46. L. C. Kong, Z. P. Qin, G. Q. Xie, Z. N. Guo, H. Zhang, P. Yuan, and L. J. Qian, Laser Phys. Lett. **13**, 045801 (2016).
47. P. G. Ge, J. Liu, S. Z. Jiang, Y. Y. Xu, and B. Y. Man, Photon. Res. **3**, 256 (2015).
48. L. J. Li, H. T. Zhang, J. P. Qin, Y. L. Wang, S. S. Li, Y. J. Shen, Z. W. Lv, Y. F. Song, Y. Q. Yang, W. L. Yang, X. M. Duan, and M. H. Chen, Laser Phys. Lett. **15**, 085806 (2018).
49. X. C. Su, B. T. Zhang, Y. R. Wang, G. B. He, G. R. Li, N. Lin, K. J. Yang, J. He, and S. D. Lu, Photon. Res. **6**, 498 (2018).